

Reversible Copper Sulfide Conversion in Nonflammable Trimethyl Phosphate Electrolytes for Safe Sodium-Ion Batteries

Huihua Li, Huang Zhang, Thomas Diemant, R. Jürgen Behm, Dorin Geiger, Ute Kaiser, Alberto Varzi,* and Stefano Passerini*

Rechargeable sodium-ion batteries are considered promising candidates for low-cost and large-scale energy storage systems. However, the limited energy density, cyclability, and safety issues remain challenges for practical applications. Herein, investigation of the $\text{Cu}_{1.8}\text{S}/\text{C}$ composite material as the negative electrode active (conversion) material in combination with a concentrated electrolyte composed of a 3.3 M solution of sodium bis(fluorosulfonyl)imide (NaFSI) in trimethyl phosphate and fluoroethylene carbonate (FEC) as the additive is reported on. Such a combination enables the stable cycling of the conversion-type $\text{Cu}_{1.8}\text{S}/\text{C}$ electrode material for hundreds of cycles with high capacity (380 mAh g^{-1}). Both the salt (NaFSI) and the additive (FEC) contribute to the formation of a stable NaF-rich solid electrolyte interphase (SEI) on the anode surface. A full cell using the $\text{Na}_3\text{V}_2(\text{PO}_4)_3/\text{C}$ cathode also demonstrates stable cycling performance for 200 cycles with a promising Coulombic efficiency (CE) (99.3%). These findings open new opportunities for the development of safer rechargeable sodium-ion batteries.

1. Introduction

Recently, large-scale energy storage technologies are receiving increasing interest as they are considered key technologies for the exploitation of renewable energy sources. Although lithium-ion batteries (LIBs) have dominated the portable electronics and electric vehicles field in recent years, their successful introduction in the market of large-scale stationary energy storage is restricted due to the limited lithium and, especially, cobalt availability.^[1] In this regard, alternative battery chemistries that are cost-effective and based on abundant elements, such as Zn-ion batteries (ZIBs) and sodium-ion batteries (SIBs), attract great interest. ZIBs have, potentially, high energy density (1218 Wh kg^{-1}) and intrinsic safety.^[2] However, they still suffer from limited

energy efficiency and a short lifespan. Thus, SIBs are emerging as the most promising alternative to LIBs due to the natural abundance and low cost of sodium, as well as the similar chemical properties of Li and Na.^[3] Indeed, the electrochemical performance of SIBs has been remarkably improved benefiting from the fast development of new high-performance electrode materials. For example, various classes of materials have been investigated for sodium storage such as layered transition metal oxides,^[4] Prussian blue analogues,^[5] and polyanionic compounds^[6] for the positive electrode (cathode), and carbon,^[7] alloying-type metals,^[8] and conversion-type materials for the negative electrode (anode). With regard to high-capacity anode materials for SIBs, metal sulfides/oxides have attracted particular interest due to their high theoretical capacity based on the conversion reaction mechanism.^[9] Among them, transition metal sulfides (TMSs, e.g., Cu_xS ,^[10] Fe_7S_8 ,^[11] SnS_2 ,^[12] MoS_2 ,^[13] Ni_3S_4 ^[14]) have demonstrated enhanced reversible capacities for sodium storage due to the weaker M–S ionic bond compared to the M–O bond, resulting in higher ionic conductivity and faster reaction kinetics.^[15] Copper sulfides (Cu_xS), as typical members of the TMS family, have been widely investigated in applications for solar cells,^[16] photocatalysis,^[17] gas sensors,^[18] and electrochemical energy storage.^[10] For example, digenite $\text{Cu}_{1.8}\text{S}$ could well serve as the anode material for both LIBs and SIBs.^[19]

H. Li, Prof. H. Zhang, Dr. T. Diemant, Prof. R. Jürgen Behm, Dr. A. Varzi, Prof. S. Passerini

Helmholtz Institute Ulm (HIU)

Helmholtzstrasse 11, D-89081 Ulm, Germany

E-mail: alberto.varzi@kit.edu; stefano.passerini@kit.edu

H. Li, Prof. H. Zhang, Dr. A. Varzi, Prof. S. Passerini

Karlsruhe Institute of Technology (KIT)

P.O. Box 3640, D-76021 Karlsruhe, Germany

Dr. T. Diemant, Prof. R. Jürgen Behm

Institute of Surface Chemistry and Catalysis

Ulm University

Albert-Einstein-Allee 47, D-89081 Ulm, Germany

Dr. D. Geiger, Prof. U. Kaiser

Central Facility for Electron Microscopy

Group of Electron Microscopy of Materials Science

Ulm University

Albert-Einstein-Allee 11, 89081 Ulm, Germany

 The ORCID identification number(s) for the author(s) of this article can be found under <https://doi.org/10.1002/ssstr.202100035>.

© 2021 The Authors. Small Structures published by Wiley-VCH GmbH. This is an open access article under the terms of the Creative Commons Attribution-NonCommercial-NoDerivs License, which permits use and distribution in any medium, provided the original work is properly cited, the use is non-commercial and no modifications or adaptations are made.

DOI: 10.1002/ssstr.202100035

Meanwhile, electrolytes play a crucial role with regard to battery performance and safety too. Current SIB electrolyte research focuses mainly on volatile, flammable, and voltage-sensitive solvents, namely, carbonate or ether-based electrolytes.^[20] This means that, analogously to LIBs, SIBs may suffer from risk of fire in case of accident or misuse (e.g., overcharge). This risk may even be higher than in LIBs, considering the highest reactivity of sodium metal. To address the safety issue of batteries, the simplest yet widely investigated strategy is to use ionic liquids or solid-state electrolytes. However, the low ionic conductivity at room temperature of the former and the high electrode/electrolyte interfacial resistance of the latter may affect their practical application.^[21] Consequently, it is very important to develop safe, nonflammable liquid electrolytes with comparable ionic conductivity and interfacial resistance as obtained for the current organic carbonate electrolytes. As reported in the literature, fluoroethers,^[22] fluorophosphate,^[23] and organosilicon compounds^[24] have been investigated as nonflammable solvents for LIBs. Moreover, the low-molecular-weight phosphate-based solvents with high solubility of Li and Na salts are particularly promising as they could enable an ionic conductivity comparable to that of carbonate-based electrolytes. As a matter of fact, triethyl phosphate (TEP),^[25] trimethyl phosphate (TMP),^[26] dimethyl methyl phosphonate (DMMP),^[27] and diethyl ethyl phosphonate (DEEP)^[28] have been reported as electrolyte solvents that are compatible with carbon-based electrodes in both LIBs and SIBs. In particular, TMP appears to be the most appropriate choice for safe electrolytes due to its low viscosity (2.3 mPa s), high dielectric constant (21.6), wide liquid temperature range (between -46 and 197 °C), and chemical stability.^[3b,29] In the electrolyte, the phosphorous atoms of TMP can act as a trap for hydrogen radicals, which are the initiators of chain reactions leading to combustion.^[29a] However, the decomposition of TMP at a low operating potential does not result in the formation of a stable solid electrolyte interphase (SEI) film on the anode's surface, which hinders its use with low-voltage anode materials.^[30] In this respect, film-forming additives have been incorporated into the electrolytes to suppress TMP decomposition.^[30b] It was proven that the use of a fluoroethylene carbonate (FEC) additive can enhance the electrochemical compatibility of TMP with the anode, enabling reversible Na storage in hard carbon anodes for intrinsically safe SIBs.^[26] For example, Zeng et al. reported the TMP-based electrolyte with FEC additive to be completely nonflammable.^[3b] Hard carbon electrodes showed high reversible capacity and capacity retention in TMP+FEC. The excellent electrochemical performance mainly comes from the formation of a stable SEI film, which effectively hinders unfavorable side reactions. High salt concentrations have been shown to be promising for the stabilization of TMP-based nonflammable electrolytes for hard carbon anode materials, benefiting from the formation of stable anion-derived SEI films on the electrode.^[31] For example, Liu et al. used a hard carbon anode and a nonflammable TMP electrolyte to construct an intrinsically safe Na-ion battery. In this case, an increased molar ratio of $\text{NaClO}_4/\text{TMP}$ and the addition of an SEI film-forming additive FEC was proven to be beneficial.^[26] Similarly, a highly concentrated $\text{NaN}(\text{SO}_2\text{F})_2/\text{TMP}$ electrolyte facilitates the formation of a robust inorganic passivation film, allowing reversible sodium insertion/extraction in hard carbon, while having flame-retardant properties.^[29a]

However, most of the reports on TMP-based nonflammable electrolytes focus only on hard carbon/graphite anodes. There are rare results reported on conversion-based materials in TMP electrolytes for SIBs.

In this work, we report for the first time the reversible conversion of a copper-sulfide material in a nonflammable phosphate-based electrolytes for safe and high-energy SIBs. The metal-organic framework (MOF)-derived $\text{Cu}_{1.8}\text{S}$ is used as the active anode material in combination with an electrolyte consisting of 3.3 M sodium bis(fluorosulfonyl)imide (NaFSI) in TMP with 5 wt% FEC as additive. The results demonstrate that a NaF-rich SEI is formed, allowing a stable conversion reaction. The $\text{Cu}_{1.8}\text{S}/\text{C}$ anode has a promising electrochemical performance with high reversible capacity, excellent rate capability, and long cycling stability. Full Na-ion cells featuring $\text{Na}_3\text{V}_2(\text{PO}_4)_3/\text{C}$ as the positive electrode show excellent cycling stability over 200 cycles, supporting our strategy to develop safer SIBs.

2. Results and Discussion

2.1. Material Synthesis and Characterization

Figure 1a schematically shows the facile solution-based synthesis route used to synthesize the Cu-1,3,5-benzenetricarboxylic acid (BTC) precursor followed by its direct sulfidation and carbonization yielding to the $\text{Cu}_{1.8}\text{S}/\text{C}$ composite. The crystal structure of the precursor was identified by powder X-ray diffraction (XRD), as shown in the representative powder diffractogram in Figure S1, Supporting Information, which demonstrates the Cu-BTC to possess a cubic structure.^[32] After sulfidation of Cu-BTC, the XRD pattern of the final composite (see Figure 1b) evidences the formation of the digenite $\text{Cu}_{1.8}\text{S}$ phase (JCPDS NO. 24-0061), in which the four main peaks located at 27.7° , 32.1° , 46.1° , and 54.6° reflect the (111), (200), (220), and (311) planes, respectively. No diffraction peaks from the Cu-BTC and S precursors are detected, indicating that the Cu-BTC was completely converted into $\text{Cu}_{1.8}\text{S}$ and no crystalline sulfur precursors remained after the high-temperature treatment (characteristic S peak $2\theta = 23^\circ$). In addition, no evident carbon-related peak could be found in the XRD pattern, probably due to the low crystallinity of the carbonaceous framework. Raman spectroscopy was used to analyze the nature of the carbon, as shown in Figure S2, Supporting Information. The two broad peaks located at 1380 and 1535 cm^{-1} are characteristic of the D and G bands of disordered carbon and graphitized carbon, respectively, indicating that the carbonaceous network is not fully graphitized.^[10,11] In addition, the specific surface area and pore size distribution of Cu-BTC and $\text{Cu}_{1.8}\text{S}/\text{C}$ were determined from N_2 adsorption-desorption isotherms by multipoint Brunauer-Emmett-Teller (BET) analysis (Figure S3, Supporting Information). Specific surface areas were determined to be $\approx 795.8\text{ m}^2\text{ g}^{-1}$ for Cu-BTC and $20.2\text{ m}^2\text{ g}^{-1}$ for $\text{Cu}_{1.8}\text{S}/\text{C}$ (Figure S3a,b, Supporting Information). The pore size distribution results demonstrate that the Cu-BTC exhibits a micro-mesoporous structure, whereas the $\text{Cu}_{1.8}\text{S}/\text{C}$ composite has mostly a macroporous character (Figure S3c,d, Supporting Information). Thermogravimetric (TGA) analysis of the $\text{Cu}_{1.8}\text{S}/\text{C}$ composite was conducted by heating in O_2 from 30 to 1000 °C (Figure S4a, Supporting Information) to determine

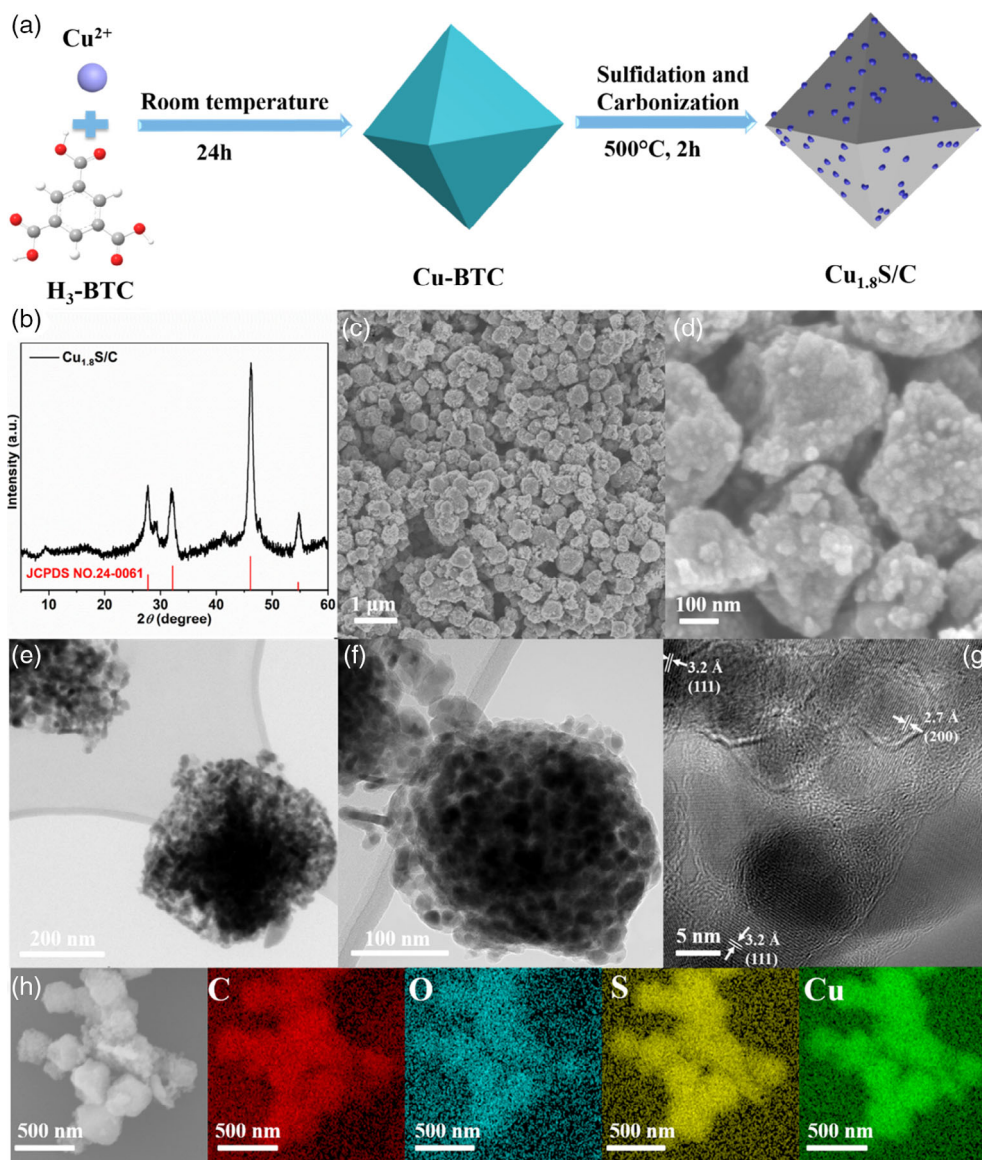


Figure 1. a) Schematic illustration of the synthetic procedure used to obtain the Cu–BTC precursor and the final $\text{Cu}_{1.8}\text{S}/\text{C}$ composite. b) Powder XRD pattern of $\text{Cu}_{1.8}\text{S}/\text{C}$. c–h) Morphological and structural features of the $\text{Cu}_{1.8}\text{S}/\text{C}$ composite. (c,d) SEM images of $\text{Cu}_{1.8}\text{S}/\text{C}$. (e–g) High-resolution TEM (HR-TEM) images of $\text{Cu}_{1.8}\text{S}/\text{C}$ with different magnifications. (h) Elemental maps of $\text{Cu}_{1.8}\text{S}/\text{C}$ by SEM-EDX.

the $\text{Cu}_{1.8}\text{S}$ and carbon content. The combustion product collected after the TGA measurement was characterized by XRD (Figure S4b, Supporting Information) and determined to be CuO . According to this, the weight percentage of $\text{Cu}_{1.8}\text{S}$ in the composite is estimated to be $\approx 67\%$ (see the Supporting Information for a detailed discussion of the combustion mechanism and calculations). Scanning electron microscopy (SEM) and transmission electron microscopy (TEM) were used to further characterize the morphology and structure of the Cu–BTC and $\text{Cu}_{1.8}\text{S}/\text{C}$. As previously mentioned, the Cu–BTC precursor has a cubic (fcc) crystallographic structure and aggregates into octahedrons with a uniform size of about 400 nm (Figure S5, Supporting Information). As shown in Figure 1c,d, the $\text{Cu}_{1.8}\text{S}/\text{C}$ composite maintains the parental morphology of Cu–BTC. The

microstructure of $\text{Cu}_{1.8}\text{S}/\text{C}$ was further characterized by TEM. As shown in Figure 1e,f, the $\text{Cu}_{1.8}\text{S}$ nanoparticles with an average size of ≈ 8 nm are homogeneously embedded in the carbon matrix. The high-resolution TEM image in Figure 1g shows the lattice fringes of the (111) and (200) planes with a d spacing of 3.2 and 2.7 Å, respectively. The energy dispersive X-ray spectroscopy (EDX) mapping shown in Figure 1h further shows the uniform distribution of C, O, S, and Cu in the $\text{Cu}_{1.8}\text{S}/\text{C}$ composite.

2.2. Physicochemical Properties of TMP-Based Nonflammable Electrolytes

Electrolyte flammability can deeply affect battery safety. To verify the flammability of the TMP-based electrolytes, a direct ignition

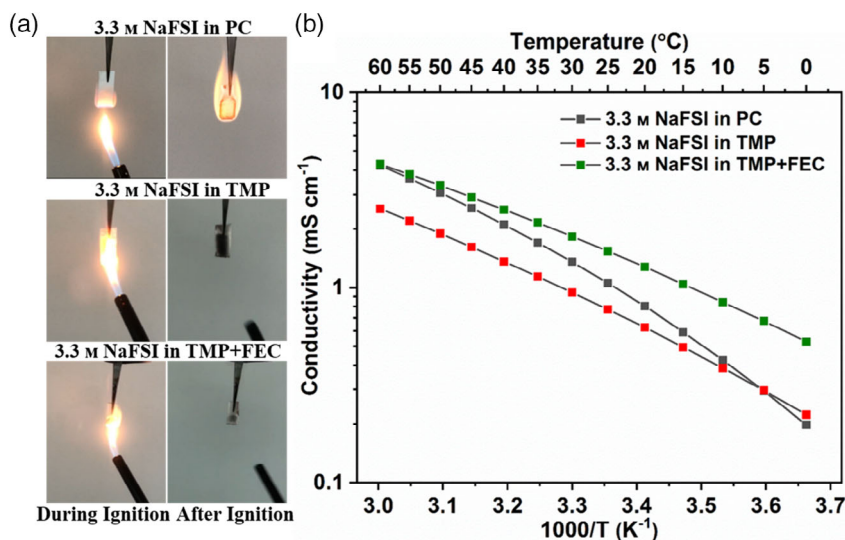


Figure 2. Physicochemical properties of the electrolytes. a) Flame test of glass fiber separators soaked with the electrolytes. b) Temperature-dependence ionic conductivity of the electrolytes.

experiment was performed. **Figure 2a** and Supporting Videos 1, 2, 3 show the flammability of 3.3 M NaFSI-PC, 3.3 M NaFSI-TMP, and 3.3 M NaFSI-TMP+FEC. The images as well as the movies clearly indicate that, even when in direct contact with the flame, the TMP-based electrolytes do not ignite, whereas the conventional carbonate electrolyte burns spontaneously after ignition. This result confirms the strong fire retardancy effect of TMP even with the FEC additive. The ionic conductivity of 3.3 M NaFSI-PC, 3.3 M NaFSI-TMP, and 3.3 M NaFSI-TMP+FEC, measured at temperatures between 0 and 60 °C are shown in **Figure 2b**. The 3.3 M NaFSI-TMP electrolyte exhibits the lowest ionic conductivity at almost any temperature. The addition of FEC (3.3 M NaFSI-TMP+FEC) leads to a remarkable increase of the conductivity at all temperatures (in particular, 1.5 mS cm⁻¹ at room temperature and 0.5 mS cm⁻¹ at 0 °C). Finally, the 3.3 M NaFSI-PC electrolyte achieves a conductivity value at 60 °C comparable to that of 3.3 M NaFSI-TMP+FEC, which drops at 0 °C below that of the 3.3 M NaFSI-TMP electrolyte. The temperature-dependent ionic conductivity of all electrolyte systems is described by the Vogel–Tamman–Fulcher (VTF) equation (**Figure S6**, Supporting Information). The VTF parameters for this system are shown in **Table S1**, Supporting Information. Based on the VTF fitting, the activation energies of the electrolytes were calculated to be 0.055, 0.088, and 0.076 eV for 3.3 M NaFSI-PC, 3.3 M NaFSI-TMP, and 3.3 M NaFSI-TMP+FEC, respectively. Therefore, FEC has clearly a beneficial effect with regard to ionic transport in the electrolyte.

The ion coordination in the TMP- and carbonate-based electrolytes was studied using Raman spectroscopy (**Figure 3a,b**). On the basis of the deconvolution analysis (**Figure 3a**), the Raman spectrum of neat TMP shows two peaks at 737 and 753 cm⁻¹ corresponding to the symmetric P–O–C stretching.^[33] The intensity of these two peaks gradually decreases and their positions shift as the Na salt concentration increases from 1 to 3.3 M. Meanwhile, a new peak at 746 cm⁻¹ emerges in the TMP-based electrolytes due to the symmetric P–O–C stretching of

Na⁺-solvated TMP molecules. These changes demonstrate the strong interaction between TMP molecules and Na⁺ ions.^[34] As shown in **Figure 3b**, the Raman spectrum of FSI⁻ contains two peaks at 1221 and 1226 cm⁻¹ arising from the contact ion pairs (CIPs; FSI⁻ coordinated with one Na⁺ ion) and aggregates (AGGs; FSI⁻ coordinated with two or more Na⁺ ions), respectively.^[35] In the diluted electrolyte (1 M NaFSI-TMP), most of the FSI⁻ is either free (1212 cm⁻¹) or in solvent-separated ion pairs (1217 cm⁻¹), with small amounts of CIPs and AGGs.^[36] As the Na salt concentration increases from 1 to 3.3 M, the signals of CIPs and AGGs increase, whereas those of the free FSI⁻ and solvent-separated ion pairs decrease. Due to the small amount of FEC addition, negligible changes of AGGs are observed in 3.3 M NaFSI-TMP+FEC. Representative Na⁺ cation solvated species in the diluted (1 M) and concentrated (3.3 M) solutions are schematically shown in **Figure 3c**. In the diluted electrolyte, a stable solvation structure around Na⁺ is recorded with three or fourfold coordination; however, free TMP and FSI⁻ are present.^[35,36] However, in the concentrated electrolyte system, almost all TMP and FSI⁻ strongly coordinate to Na⁺ cations.

2.3. Electrochemical Performance

The electrochemical properties of the Cu_{1.8}S/C anode in TMP- and carbonate-based electrolytes are compared in **Figure 4**. **Figure 4a** and **Figure S7**, Supporting Information, show the cyclic voltammograms (CVs) of Cu_{1.8}S/C electrodes recorded at a scan rate of 0.05 mV s⁻¹ between 0.01 and 3.0 V (vs Na⁺/Na) in the various electrolytes. The CV curves evidence comparable electrochemical behavior, with the typical signatures of copper sulfide conversion reaction with sodium. Galvanostatic charge–discharge (GCD) voltage profiles of the Cu_{1.8}S/C half-cells were also recorded at 0.1 A g⁻¹ in the same voltage range (**Figure 4b** and **Figure S8**, Supporting Information). Despite the higher initial capacity, the Cu_{1.8}S/C electrodes tested in the 3.3 M NaFSI-PC and 3.3 M NaFSI-TMP electrolytes show

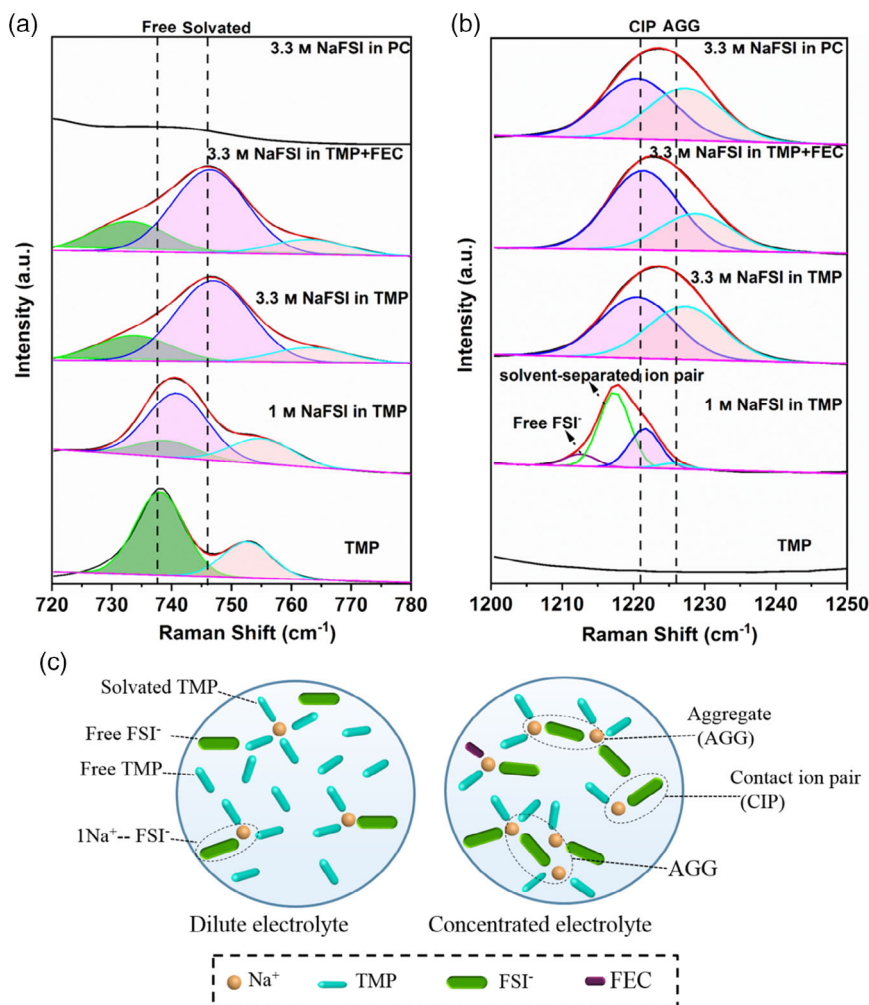


Figure 3. Raman spectra of 3.3 M NaFSI-PC, 3.3 M NaFSI-TMP, and 3.3 M NaFSI-TMP+FEC: a) 720–780 cm^{-1} region and b) 1200–1250 cm^{-1} region. c) Schematic illustration representative of the Na^+ environment in the diluted (i.e., 1 mol L^{-1}) and concentrated (i.e., 3.3 mol L^{-1}) electrolytes.

an obvious fading in the first 20 cycles. In contrast, the electrode tested in the TMP-based electrolyte + FEC additive exhibits very stable cycling. The electrode delivered initial sodiation and desodiation capacities of 617 and 431 mAh g^{-1} , respectively, corresponding to an initial CE of 70%. After the first cycle, the $\text{Cu}_{1.8}\text{S}/\text{C}$ in 3.3 M NaFSI-TMP+FEC displays almost overlapping voltage profiles, indicating the high cycling stability. This is further confirmed by the long-term cycling measurement at a current density of 0.1 A g^{-1} (Figure 4c), in which the reversible Na storage capacity (CE of $\approx 99.5\%$) of $\text{Cu}_{1.8}\text{S}/\text{C}$ in 3.3 M NaFSI-TMP+FEC is stable at 365 mAh g^{-1} after 140 cycles, which is substantially higher than that observed in 3.3 M NaFSI-PC (57 mAh g^{-1} after 140 cycles) and 3.3 M NaFSI-TMP (207 mAh g^{-1} after 120 cycles). These results indicate that FEC can significantly enhance the cycling performance of the conversion-type $\text{Cu}_{1.8}\text{S}/\text{C}$ electrode in the nonflammable TMP electrolyte, acting as a highly efficient SEI-forming additive. Apart from its excellent cycling stability, the $\text{Cu}_{1.8}\text{S}/\text{C}$ in 3.3 M NaFSI-TMP+FEC also exhibits good rate performance. As shown in Figure 4d,e, the electrode exhibits discharge capacities of 441, 392, 309, 221, and 138 mAh g^{-1} at

current densities of 0.1, 0.2, 0.5, 1, and 2 A g^{-1} , respectively. When going back to 0.1 and 0.2 A g^{-1} , a capacity comparable to the initial values is recovered by the $\text{Cu}_{1.8}\text{S}/\text{C}$ electrode. Differently, the electrodes show an inferior performance in the 3.3 M NaFSI-PC and 3.3 M NaFSI-TMP electrolyte (Figure S9, Supporting Information). Finally, long-term cycling tests at a relatively high current density of 1 A g^{-1} were also performed for 200 cycles (after 10 cycles at 0.1 A g^{-1} for activation) in different electrolytes (Figure 4f). The cell with the 3.3 M NaFSI-TMP+FEC electrolyte can still deliver 213 mAh g^{-1} after 200 cycles, corresponding to a relatively low capacity loss of about 0.1% per cycle. In contrast, the $\text{Cu}_{1.8}\text{S}/\text{C}$ electrodes in 3.3 M NaFSI-PC and 3.3 M NaFSI-TMP show fast fading with remaining capacities of only 26 and 50 mAh g^{-1} after 200 cycles, respectively. To further understand the influence of the electrolyte composition on the electrochemical performance, the voltage profiles of $\text{Cu}_{1.8}\text{S}/\text{C}$ in 3.3 M NaFSI-PC, 3.3 M NaFSI-TMP, and 3.3 M NaFSI-TMP+FEC are displayed in Figure S10, Supporting Information. In the first 50 cycles, the characteristic features of copper sulfide entirely disappear in 3.3 M NaFSI-PC

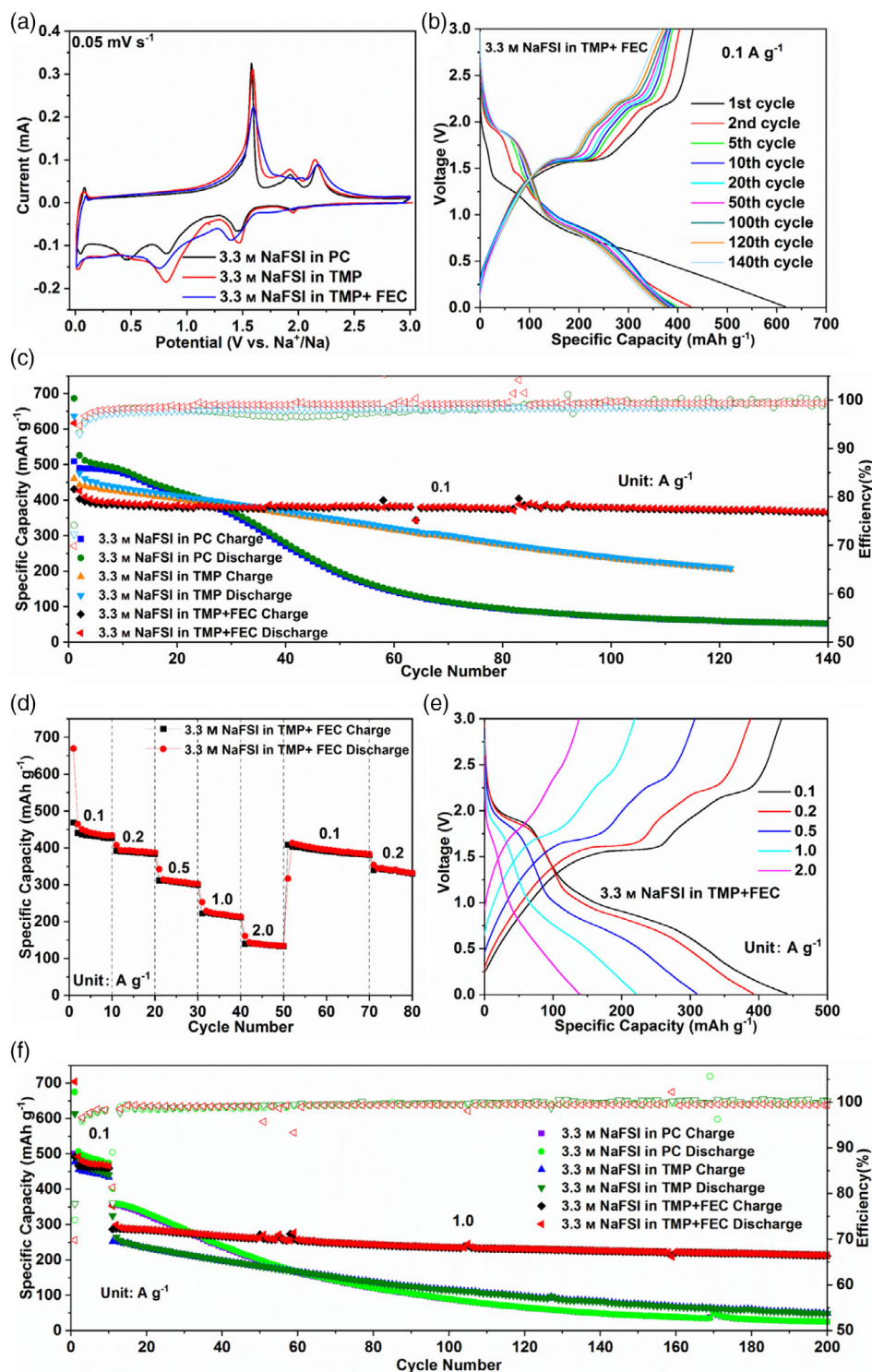


Figure 4. Electrochemical characterization of Cu_{1.8}S/C electrodes in 3.3 m NaFSI-PC, 3.3 m NaFSI-TMP, and 3.3 m NaFSI-TMP+FEC. a) CVs showing the first cycle at a scan rate of 0.05 mV s⁻¹ in the potential range from 0.01 and 3.0 V versus Na/Na⁺. b) Selected charge and discharge profiles in 3.3 m NaFSI-TMP+FEC at 0.1 A g⁻¹ (1st, 2nd, 5th, 10th, 20th, 50th, 100th, 120th, and 140th cycle). c) Cycling performance at 0.1 A g⁻¹. d) Rate performance in 3.3 m NaFSI-TMP+FEC at various current densities, ranging from 0.1 to 2.0 A g⁻¹. e) Galvanostatic discharge-charge profiles in 3.3 m NaFSI-TMP+FEC at different current densities, ranging from 0.1 to 2.0 A g⁻¹ for selected cycles (i.e., the 5th, 15th, 25th, 35th, and 45th). f) Cycling performance at 1 A g⁻¹ for 200 cycles (after 10 cycles at 0.1 A g⁻¹ in the beginning as an activation step).

and 3.3 M NaFSI-TMP, leading to a rapid capacity fading. Although the exact reason is unknown, formation of polysulfides cannot be entirely excluded, especially in the PC-based electrolyte.^[37] In contrast, the low binding energy of sodium polysulfides with FEC may restrict their dissolution. This would be in line with the superior electrochemical performance of Cu_{1.8}S/C in the 3.3 M NaFSI-TMP+FEC electrolyte. Furthermore, a comparison of the electrochemical performance of Cu_{1.8}S/C with that of hard carbon (BELLFINE LN0001, AT Electrode, see the Experimental Section in the Supporting Information) in 3.3 M NaFSI-TMP+FEC is reported in Figure S11, Supporting Information. The Cu_{1.8}S/C clearly possesses a higher specific capacity than the hard carbon, both per unit of weight and volume. The sodium storage performance of Cu_{1.8}S/C is comparable and even superior to that of previous copper sulfides reported in the literature (see list in Table S2, Supporting Information). Overall, the aforementioned electrochemical performance tests clearly demonstrate the highly reversible electrochemistry of Cu_{1.8}S/C electrodes in the optimized nonflammable TMP-based electrolytes, which could be very promising for the fabrication of safe and high-energy SIBs.

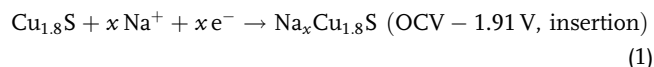
2.4. Mechanism and Interface Investigation

To learn more about the electrochemical reaction mechanism and the structural evolution of Cu_{1.8}S/C in the 3.3 M NaFSI-TMP+FEC electrolyte, in situ XRD measurements were performed during the first sodiation/desodiation cycle. The voltage profile and the corresponding XRD patterns (126 scans) upon the first galvanostatic discharge-charge cycle are shown in Figure 5a,b. Looking at the XRD patterns, the first cycle can be divided into four different regions. As the sodiation process begins (region 1, from open-circuit voltage (OCV) to 1.91 V), the two peaks at 27.7° and 32.1° (Figure S12a, Supporting Information) gradually shift to lower angles (27.5° and 31.9°), indicating the crystal structure expansion as a result of Na⁺ insertion into Cu_{1.8}S (Equation (1)). Upon further sodiation (region 2 from 1.91 to 1.45 V, Figure 5c), two new peaks at 32.5° and 39.3° appear, which can be attributed to the (311) and (321) crystal planes of a Na₃Cu₄S₄ phase (JCPDS NO. 71-1292) in agreement with Equation (2) and previous literature reporting the Na₃Cu₄S₄ phase formation upon Na⁺ uptake into Cu_{1.8}S.^[38] Finally, at even lower voltage values (region 3 from 1.45 to 0.01 V, Figure S12b, Supporting Information), two new diffraction peaks appear at 23.5° and 38.9°. These can be attributed to the (111) and (220) crystal planes of Na₂S (JCPDS No. 23-0441), which is the final product of the conversion reaction (Equation (3)). At the same time, the intense characteristic peak of Cu⁰ (43.5°, JCPDS No. 04-0836) appears, which corroborates the complete conversion reaction of Cu_{1.8}S into Cu⁰ and Na₂S. Sodiation and desodiation of carbon at low potential (<0.3 V) may also occur (Equation (4) and (5)).^[11] However, due to the low crystallinity of the carbonaceous framework, no obvious carbon-related peaks are detected in the XRD patterns. Upon desodiation (region 4 from 0.01 to 3.0 V), the peaks of Na₂S and Cu⁰ gradually vanish and a weak peak at 32.5° emerges, confirming the re-formation of the Na₃Cu₄S₄ phase (Figure 5d, Equation (6)). Meanwhile, the features corresponding to Na₂S and Cu⁰ are still detected even at full state of charge, indicating that the complete desodiation is not

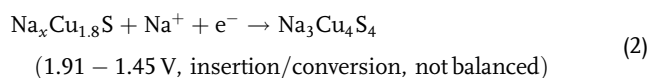
achieved during the in situ XRD measurement. To visualize the evolution of the morphology and structure of Cu_{1.8}S/C upon cycling, detailed ex situ SEM and TEM investigations were conducted after 100 cycles (Figure S12c,d, Supporting Information and Figure 5e,f). The ex situ SEM images (Figure S12c,d, Supporting Information) demonstrate that the octahedral particle morphology of the Cu_{1.8}S/C composite is still well retained. The TEM image in Figure 5e also confirms the retained particle morphology without substantial structural deterioration, indicating that the carbon framework can efficiently buffer the volume variation upon multiple (de)sodiation cycles. Figure 5f shows an HR-TEM image of Cu_{1.8}S/C after 100 cycles. Only one new phase with a *d* spacing of 7.31 Å, indexed to the Na₃Cu₄S₄ (JCPDS NO. 71-1292) phase, can be observed. The result is consistent with the in situ XRD results, which furthermore evidence that the original Cu_{1.8}S phase cannot be recovered. Overall, the first-cycle (de)sodiation reaction process of Cu_{1.8}S/C in 3.3 M NaFSI-TMP+FEC can be summarized as follows:

For discharge

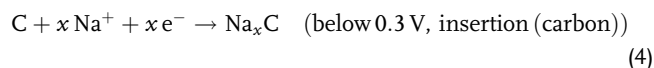
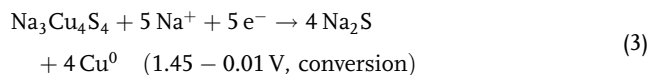
Region 1



Region 2

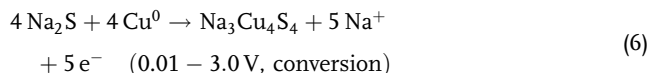
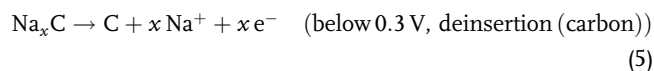


Region 3



For charge

Region 4



The chemical composition and the abundance of functional groups on the surface of the Cu_{1.8}S/C electrodes was also studied by X-ray photoelectron spectroscopy (XPS) to gain more information about the SEI. Figure 6a (and Figure S13, Supporting Information) shows the results of measurements performed on electrodes after the first full sodiation in the different electrolytes. For comparison purposes, also shown are the XPS results gained on a pristine electrode, which is the starting point of our discussion. The C 1s detailed spectrum of the pristine electrode shows four peaks at 284.8, 286.2, 288.5, and 290.9 eV. The first peak is assigned to C—C—H species (284.8 eV), including the conductive carbon additive/framework in the electrode material.^[11] The second one (286.2 eV) is a convolution of the contributions from C—O species and the CH₂ groups of the PVDF

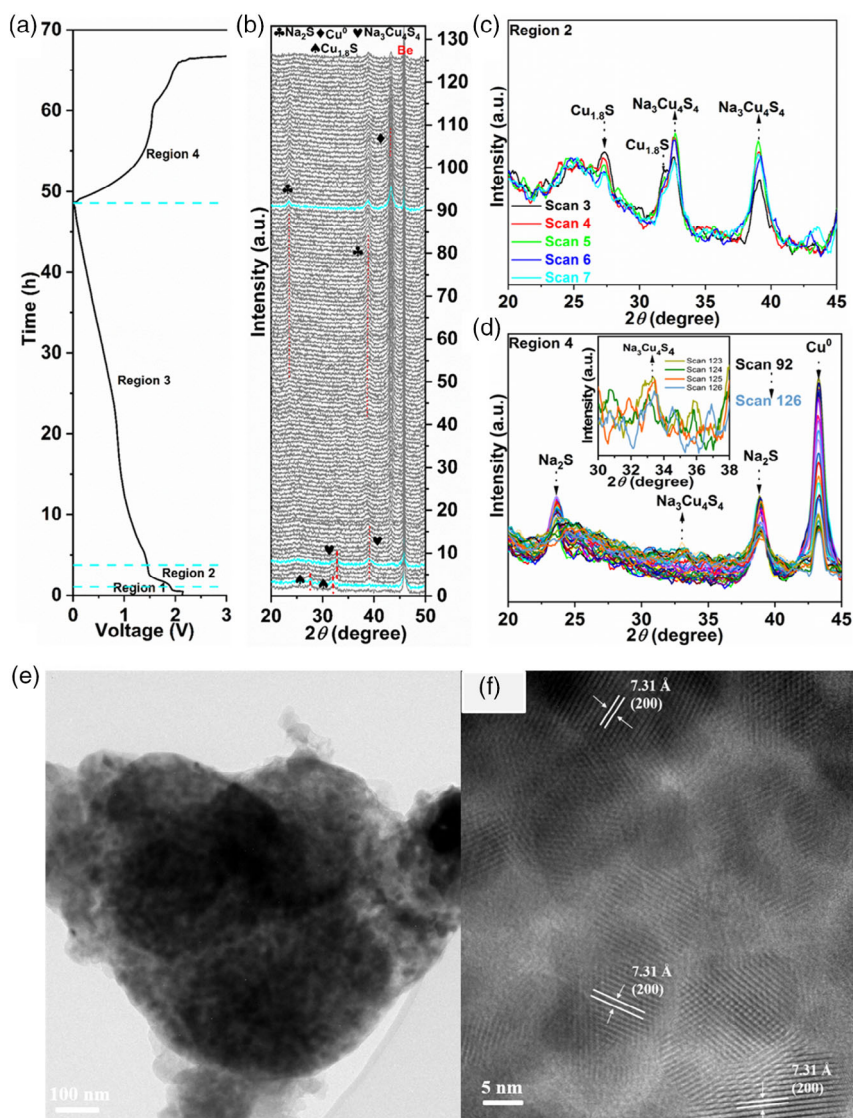


Figure 5. Reaction mechanism analysis of $\text{Cu}_{1.8}\text{S}/\text{C}$ -based electrodes in 3.3 m NaFSI-TMP+FEC. a) First sodiation/desodiation voltage profile. b) Waterfall plot of the XRD patterns recorded consecutively during (dis-)charge (scans 1–126). Selected regions of the waterfall plot: c) region 2, scans 3–7. d) region 4, scans 92–126. e,f) (HR)-TEM images of the $\text{Cu}_{1.8}\text{S}/\text{C}$ composite recorded after 100 cycles in 3.3 m NaFSI-TMP +FEC.

binder, whereas the third and fourth peak can be assigned to C=O species and the CF_2 groups of the PVDF binder, respectively.^[39] The spectrum in the S $2p$ region is dominated by two peak doublets, which are attributed to $\text{Cu}_{1.8}\text{S}$ (S $2p_{3/2}$ peak at 162.1 eV) and C—S—C species in the carbonaceous framework (S $2p_{3/2}$ peak at 164.2 eV), respectively.^[11,19] In addition, the two smaller peak doublets at higher binding energy are attributed to oxidized S species (sulfites or equivalent species at 166.7 and 167.9 eV) and sulfates (168.8 and 170.2 eV).^[40] The O $1s$ spectrum contains two peaks, which are mainly assigned to C=O (531.8 eV) and C—O (533.3 eV) moieties. It may be noted that the O atoms of oxidized S species will most probably also contribute to the first peak.^[40] Finally, the F $1s$ spectrum shows a single peak at 687.9 eV due to the PVDF binder.

The measurements of the cycled samples demonstrate for all electrolyte formulations the formation of a stable SEI layer after

the first sodiation. More precisely, the disappearance of the features due to $\text{Cu}_{1.8}\text{S}$ in the S $2p$ (and Cu $2p$; cf. Figure S13, Supporting Information) spectra indicates the surface layer to be thicker than 4 nm (when assuming an inelastic mean free path of about 2 nm and taking into account the detection angle of 45°). Instead, oxidized S species dominate the spectra in the S $2p$ range. Most interestingly, however, undecomposed FSI^- (S $2p_{3/2}$ peak at 170.3 eV)^[41] is only detected for the sample with 3.3 m NaFSI-TMP+FEC, whereas features due to (partly) decomposed FSI^- (S $2p_{3/2}$ peaks at ~ 167 eV and ~ 169 eV) are observed in all cases. This finding seems to indicate a stabilization of FSI^- in the SEI layer formed by cycling in NaFSI-TMP+FEC, and indeed the FSI^- -related peak doublet is still present in the S $2p$ spectrum after prolonged cycling (10 cycles; Figure S14, Supporting Information). The comparison of the results in the C $1s$ range shows a smaller amount of C—C/C—H species for

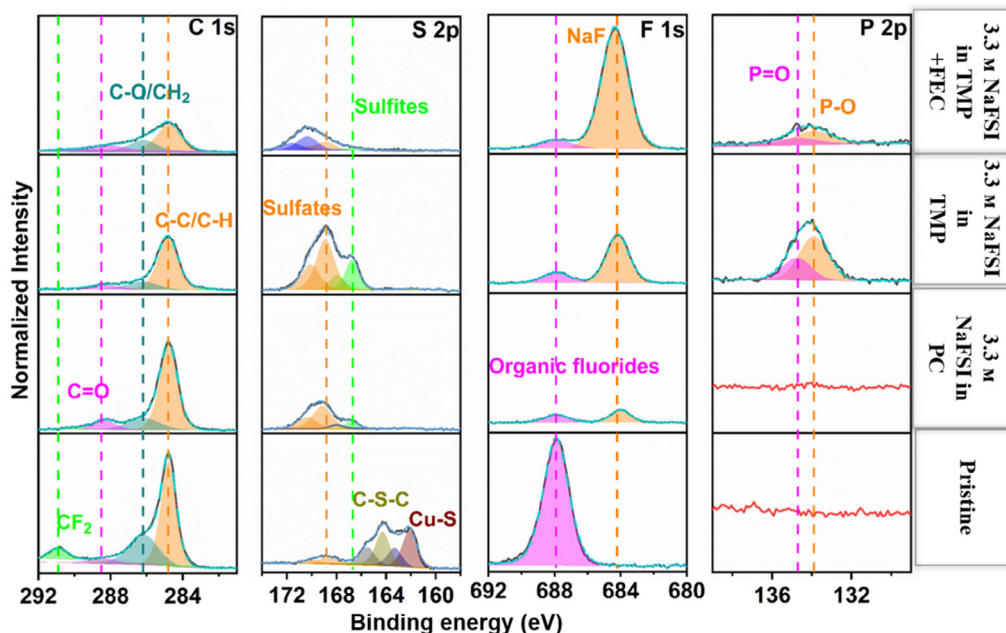


Figure 6. XPS spectra of the C 1s, S 2p, F 1s, and P 2p regions, collected from the pristine electrode and $\text{Cu}_{1.8}\text{S}/\text{C}$ electrodes after the first sodiation in 3.3 M NaFSI-PC, 3.3 M NaFSI-TMP, and 3.3 M NaFSI-TMP+FEC electrolytes at 0.1 A g^{-1} .

the NaFSI-TMP+FEC sample, while the amount of C—O and C=O species is between that of NaFSI-TMP and NaFSI-PC. The analysis of the spectra in the O 1s range is complicated by the presence of Na KLL Auger features (at $\approx 536 \text{ eV}$). The F 1s spectra of all cycled samples show two peaks at 684.2 and 687.9 eV, which can be assigned to NaF (684.2 eV)^[42] and FSI^- (687.9 eV),^[41] respectively (the latter presumably together with partial decomposition products in which the S—F bond is still intact). While FEC or its reaction products might also have a small contribution to the second peak, PVDF should not play a role anymore after SEI formation (cf. also the disappearance of the related peak at 290.9 eV in the C 1s spectra). A comparison of the peak intensities reveals the presence of a much larger amount of NaF in the SEI layer of the 3.3 M NaFSI-TMP+FEC sample. Furthermore, even after ten cycles the NaF-rich inorganic SEI layer can be still identified on the surface of the $\text{Cu}_{1.8}\text{S}/\text{C}$ electrode cycled in 3.3 M NaFSI-TMP+FEC (Figure S14, Supporting Information). Finally, it may be noted that the inclusion of TMP (and its decomposition products) in the SEI layer is corroborated by the detection of a P 2p peak doublet (P $2p_{3/2}$ peak at 133.9 eV) for the TMP-containing electrolytes.^[43] For the TMP-based electrolyte with FEC additive, the content of NaF increases, indicating that the preferential defluorination and decomposition of FEC helps in generating a NaF-rich SEI.^[25,44] Taken together, the SEI layer of the $\text{Cu}_{1.8}\text{S}/\text{C}$ electrodes in 3.3 M NaFSI-TMP+FEC after cycling contains a smaller amount of organic compounds and more NaF, suggesting a dense inorganic SEI layer. Furthermore, the FSI^- decomposition seems to be hindered by FEC addition. Overall, these XPS results demonstrate that FEC in TMP electrolytes favors the formation of a stable SEI layer, thus effectively suppressing decomposition of FSI^- and TMP and increasing the reversibility of the electrode.

2.5. Sodium Full-Cell Performance

Sodium-ion full cells were assembled using presodiated $\text{Cu}_{1.8}\text{S}/\text{C}$ as the negative electrode, $\text{Na}_3\text{V}_2(\text{PO}_4)_3/\text{C}$ as the positive electrode, and 3.3 M NaFSI-TMP+FEC (Figure 7a) as the electrolyte. It is well known that $\text{Cu}_{1.8}\text{S}/\text{C}$, like all TMSs, has a relatively high operational potential. Therefore, coupling this type of anode material with a high-voltage cathode could compensate for the voltage loss at the full-cell level. However, currently, the choice of stable sodium-based high-voltage cathodes is still very limited. Therefore, in this work, the classical $\text{Na}_3\text{V}_2(\text{PO}_4)_3/\text{C}$ was used as the cathode material. Before the full-cell assembly, the $\text{Cu}_{1.8}\text{S}/\text{C}$ anode was precycled in a sodium half-cell to compensate for the irreversible charge consumption in the initial cycles. As shown in Figure 7b, the $\text{Na}||\text{Na}_3\text{V}_2(\text{PO}_4)_3/\text{C}$ half-cell delivers a reversible capacity of 108 mAh g^{-1} at 0.12 A g^{-1} , while the $\text{Na}||\text{Cu}_{1.8}\text{S}/\text{C}$ half-cell displays a reversible capacity of 400 mAh g^{-1} at 0.1 A g^{-1} . The full cell was tested in the voltage window of 0–3.6 V. Figure 7c shows the typical charge/discharge profile of the full cell, which delivered charge/discharge capacities of $101/100 \text{ mAh g}^{-1}$ (based on the mass of $\text{Na}_3\text{V}_2(\text{PO}_4)_3/\text{C}$) at 0.12 A g^{-1} . To better highlight the individual contributions of the anode and cathode to the dis-/charge profiles of the full cells, their potential profiles were recorded versus a sodium reference electrode (see Figure S15, Supporting Information). The comparison of the cathode and full-cell voltage profile nicely displays that the capacity of the cathode is fully exploited, as could be expected by the cathode-limited cell balancing. Moreover, the full cell exhibits an outstanding long-term cycling performance with 84 mAh g^{-1} and a CE of 99.3% after 200 cycles at 0.12 A g^{-1} . The ex situ SEM images recorded postmortem on the $\text{Cu}_{1.8}\text{S}/\text{C}$ electrode after 200 cycles in full-cell configuration (Figure S16, Supporting Information) confirm the stability of the $\text{Cu}_{1.8}\text{S}/\text{C}$

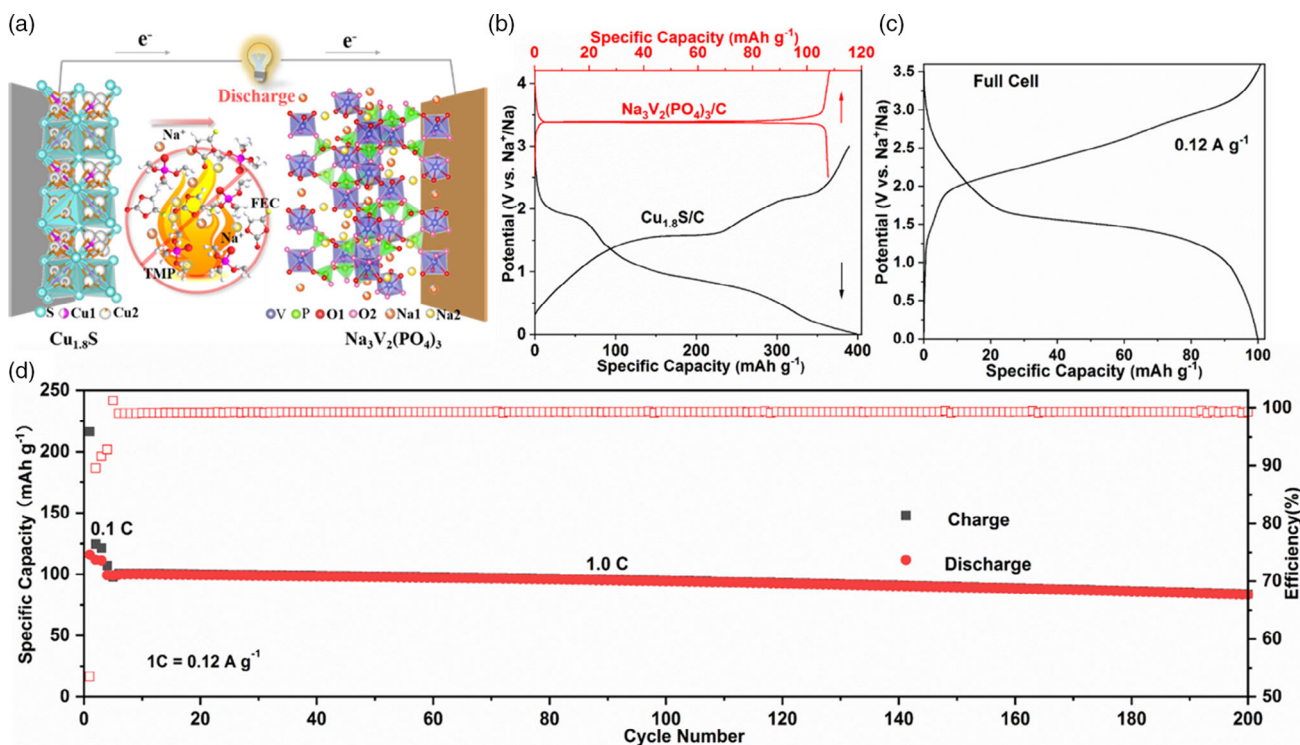


Figure 7. Electrochemical performance of a $\text{Cu}_{1.8}\text{S}/\text{C}||\text{Na}_3\text{V}_2(\text{PO}_4)_3/\text{C}$ full cell within the 0–3.6 V voltage window in the 3.3 m NaFSI-TMP+FEC electrolyte. a) Schematic illustration of $\text{Cu}_{1.8}\text{S}/\text{C}||\text{Na}_3\text{V}_2(\text{PO}_4)_3/\text{C}$ full cells. b) Characteristic charge/discharge profiles of $\text{Na}||\text{Na}_3\text{V}_2(\text{PO}_4)_3/\text{C}$ and $\text{Na}||\text{Cu}_{1.8}\text{S}/\text{C}$ half-cells. c) Galvanostatic discharge–charge profile of the full cell at 0.12 A g^{-1} . d) Long-term cycling performance at 0.12 A g^{-1} . The capacity values in panels (c) and (d) are given with respect to the $\text{Na}_3\text{V}_2(\text{PO}_4)_3/\text{C}$ weight.

composite material, as previously observed in the half-cell. These results once more confirm that combining conversion anodes and nonflammable electrolytes is a valuable strategy to achieve safe rechargeable SIBs.

3. Conclusion

In summary, the reversible conversion reaction of MOF-derived $\text{Cu}_{1.8}\text{S}/\text{C}$ in nonflammable phosphate-based electrolytes is demonstrated. A concentrated TMP electrolyte using NaFSI salt and FEC additive enables stable cycling of the $\text{Cu}_{1.8}\text{S}/\text{C}$ anode, with high reversible capacity and rate performance. Full-cell measurements, based on a $\text{Na}_3\text{V}_2(\text{PO}_4)_3$ cathode and a $\text{Cu}_{1.8}\text{S}$ anode, revealed a highly stable cycling performance with negligible capacity fading over 200 cycles. The excellent electrochemical performance is enabled by the NaF-rich SEI derived from both the salt and the FEC additive. This design strategy can be extended to various conversion materials and nonflammable electrolytes, providing a promising prospect to the further development of high-energy and safe rechargeable SIBs.

4. Experimental Section

Chemicals: $\text{Cu}(\text{NO}_3)_2 \cdot 3\text{H}_2\text{O}$ (98.0–103%) and sulfur powder (S, 99.98%) were purchased from Sigma-Aldrich. 1,3,5-Benzenetricarboxylic acid (98%) was obtained from Acros Organics. Polyvinylpyrrolidone (PVP, K30, $M_w = 44\,000\text{--}54\,000$) was purchased from

PanReac AppliChem. Methanol (98.5%) was obtained from VWR. All chemicals were directly used as received without further purification.

Synthesis of Cu–BTC Precursor: $\text{Cu}(\text{NO}_3)_2 \cdot 3\text{H}_2\text{O}$ (0.9 g) and polyvinylpyrrolidone (0.4 g; PVP, K-30) were dissolved into methanol (50 mL) to form solution A. 1,3,5-Benzenetricarboxylic acid (0.43 g, H_3BTC) was dissolved into methanol (50 mL) to form solution B. After stirring A and B for 30 min, solution B was slowly added into solution A under continuous stirring in 10 min, and then the resulting solution was kept at room temperature for 24 h. Finally, the precipitate (Cu–BTC) was collected via centrifugation, washed with methanol, and dried at 80°C overnight.

Synthesis of $\text{Cu}_{1.8}\text{S}/\text{C}$ Composite Anode Material: The $\text{Cu}_{1.8}\text{S}/\text{C}$ composite was synthesized by a one-step sulfidation and carbonization process of the Cu–BTC precursor. Cu–BTC and sulfur powder (in a mass ratio of 1:5) were put downstream and upstream in the same crucible in a tube furnace and heated to 500°C (heating ramp: 2°C min^{-1}) for 2 h under argon flow. After natural cooling to room temperature, the $\text{Cu}_{1.8}\text{S}/\text{C}$ black powder was collected.

Synthesis of $\text{Na}_3\text{V}_2(\text{PO}_4)_3/\text{C}$ Composite Cathode Material: The $\text{Na}_3\text{V}_2(\text{PO}_4)_3/\text{C}$ composite was obtained via a sol–gel method, as described earlier.^[6b] Typically, $\text{CH}_3\text{COONa} \cdot 3\text{H}_2\text{O}$ (VWR, $\geq 99\%$), $\text{NH}_4\text{H}_2\text{PO}_4$ (Alfa Aesar, $\geq 99\%$), NH_4VO_3 (Sigma-Aldrich, $\geq 99\%$), and citric acid monohydrate ($\text{C}_6\text{H}_8\text{O}_7 \cdot \text{H}_2\text{O}$) (Alfa Aesar, $\geq 99\%$) were dissolved in deionized water and dried at 80°C . After grinding, the obtained precursor was pretreated at 350°C for 6 h and then calcined at 800°C for 12 h under argon flow. After cooling, the final $\text{Na}_3\text{V}_2(\text{PO}_4)_3/\text{C}$ composite was obtained.

Preparation of the Electrolytes: The TMP solvent used in this work was purchased from Sigma-Aldrich. Before use, it was purified by redistillation under vacuum. Battery-grade sodium (I) bis(fluorosulfonyl)imide (NaFSI, 99.7%) was obtained from Solvionic. FEC and propylene carbonate (PC), both battery grade, were purchased from BASF. All electrolytes were

prepared in an argon-filled glovebox with H₂O and O₂ content lower than 0.1 ppm.

Materials Characterization: The crystalline structure of Cu–BTC and Cu_{1.8}S/C was determined by means of XRD on a Bruker D8 Advance instrument (Cu K α radiation with a wavelength of 0.154 nm). In situ XRD measurements were performed using a homemade cell featuring a Be disc as an X-ray window and current collector. The electrochemical test was controlled using a potentiostat/galvanostat (SP-150, BioLogic). The morphology and elemental composition of the materials was investigated via SEM (ZEISS 1550VP) coupled with EDX (Oxford). TEM was conducted on a Thermofisher Talos 200X. The Raman spectrum of Cu_{1.8}S/C was recorded using a confocal InVia Raman microspectrometer (Renishaw) using 633 nm laser radiation. The specific surface area and pore size distribution of Cu-MOF and Cu_{1.8}S/C were determined from nitrogen absorption–desorption isotherms (Autosorb-iQ, 3P instruments) at 77 K. TGA was performed under O₂ flow (20 cc min⁻¹) using a heating rate of 5 °C min⁻¹ (TGA-209 F, Netzsch). XPS was performed using the PHI 5800 Multitechnique ESCA system with monochromatized Al K α (1486.6 eV) radiation at a detection angle of 45° and pass energies at the analyzer of 29.35 and 93.9 eV for detail and survey spectra, respectively. The main C 1s peak of C–C/C–H species was used for binding energy calibration and set to 284.8 eV. The spectra were analyzed by a peak-fitting software (CasaXPS) using a Shirley-type background and peaks with a mixed Gaussian/Lorentzian shape. For the fit of the 2p spectra of P and S, the expected peak intensity ratio (2:1) and spin–orbit splitting (P 2p = 0.84 eV, S 2p = 1.2 eV) were fixed. The liquid Raman spectra were collected on a RAM II FT-Raman module of a Bruker Vertex70v spectrometer with a laser wavelength of 1064 nm for 1000 scans with a resolution of 2 cm⁻¹. For these measurements the samples were sealed in glass tubes containing argon gas. The ionic conductivity of the electrolytes was determined in sealed glass conductivity cells (Materials Mates 192/K1) equipped with two platinum electrodes (cell constant of 1.0 ± 0.1 cm), using a Bio-Logic conductivity meter.

Electrochemical Measurements: The anodes were made by casting slurries composed of Cu_{1.8}S/C, Super C65 (Imerys Graphite & Carbon), and polyvinylidene fluoride (Solef 6020, Solvay) in a weight ratio of 70:20:10 in N-methyl pyrrolidone (NMP, anhydrous, Sigma-Aldrich), onto a dendritic copper foil (Schlenk, 99.9%, the thickness was 18 μ m). After the initial drying in an oven at 80 °C (2 h), disk electrodes (12 mm in diameter) were punched and further vacuum-dried for 24 h at 80 °C. The average active material (Cu_{1.8}S/C) mass loading of each disk electrode was in the range between 1.2 and 1.5 mg cm⁻² (the thickness was \approx 25 μ m). The cathodes were fabricated by mixing the Na₃V₂(PO₄)₃/C with polyvinylidene fluoride, and Super C65 in a weight ratio of 80:10:10 into a slurry using NMP. This was coated onto Al foil and first dried at 80 °C overnight. Disk electrodes (12 mm in diameter) were punched from this film and vacuum-dried for 24 h at 120 °C. These disc electrodes were pressed at 5 tons cm⁻² for 10 s to increase electrode density for cell assembly. To match the negative and positive electrode capacity in the full Na-ion cell, the average active mass loadings of the anode and cathode were around 1.4 and 2.9 mg cm⁻², respectively. This resulted in an anode:cathode capacity ratio of \approx 1.25–1.35 (cathode-limited).

The half-cell galvanostatic cycling tests were performed in CR2032 coin cells, using Cu_{1.8}S/C or Na₃V₂(PO₄)₃/C as the working electrode, and sodium metal foil (Acros, 99.5%) as counter electrode. As electrolyte, 3.3 M NaFSI solution in TMP (including 5 vol% FEC as additive), 3.3 M NaFSI in TMP, and 3.3 M NaFSI in PC were used for support in a glass fiber membrane disk (GF/D, Whatman). For the Cu_{1.8}S/C||Na₃V₂(PO₄)₃/C full-cell assembly, the Cu_{1.8}S/C electrode was precycled (ten cycles at 0.1 A g⁻¹) to compensate for the initial irreversible capacity. CV experiments were conducted in three-electrode Swagelok-type cells on a VMP3 potentiostat (Biologic Science Instruments) in the potential range 0.01–3.0 V versus Na/Na⁺, using sodium metal (Acros, 99.5%) both as counter and reference electrode. All cells were assembled in an argon-filled glovebox (MBraun Labmaster; H₂O and O₂ content <0.1 ppm). The galvanostatic cycling tests were performed on a Maccor 3000 battery tester. All electrochemical tests were performed in climatic chambers at a constant temperature of 20 ± 1 °C.

Supporting Information

Supporting Information is available from the Wiley Online Library or from the author.

Acknowledgements

The authors thank Hanno Schütz for the Raman measurement and Xu Dong for the ionic conductivity measurement. The authors also thank Dr. Zhen Chen and Xu Liu for valuable discussions. H.L. gratefully acknowledges financial support from the Chinese Scholarship Council (CSC). The authors also acknowledge financial support from the Helmholtz Association and the German Ministry for Education and Research (BMBF, within the M.Era-net project “NEILLSBAT,” 03XP0120A). This work contributes to the research performed at CELEST (Center for Electrochemical Energy Storage Ulm-Karlsruhe).

Conflict of Interest

The authors declare no conflict of interest.

Authors Contributions

H.L. conceived the research idea, designed the experiments, analyzed the results, and prepared the first draft of the manuscript. H.Z. provided some research ideas, cathode materials, and helped in the analysis of Raman and XPS. T.D. and R.J.B. contributed to the characterization by XPS. D.G. and U.K. contributed to the characterization by TEM. A.V. and S.P. supervised and coordinated the work. All authors contributed to the writing and have given approval to the final version of the manuscript.

Data Availability Statement

Research data are not shared.

Keywords

conversion, copper sulfide, metal–organic frameworks, phosphate electrolytes, safety, sodium-ion batteries

Received: March 25, 2021

Revised: May 21, 2021

Published online: June 29, 2021

- [1] V. Christoph, B. Daniel, W. A. Marcel, P. Stefano, *Nat. Rev. Mater.* **2018**, *3*, 18013.
- [2] a) Y. Zhong, X. Xu, P. Liu, R. Ran, S. Jiang, H. Wu, Z. Shao, *Adv. Energy Mater.* **2020**, *10*, 2002992; b) H. Zhang, X. Liu, H. Li, I. Hasa, S. Passerini, *Angew. Chem., Int. Ed.* **2021**, *60*, 598.
- [3] a) J. Feng, Z. Zhang, L. Li, J. Yang, S. Xiong, Y. Qian, *J. Power Sources* **2015**, *284*, 222; b) Z. Zeng, X. Jiang, R. Li, D. Yuan, X. Ai, H. Yang, Y. Cao, *Adv. Sci.* **2016**, *3*, 1600066.
- [4] a) X. Liu, B. Qin, H. Zhang, A. Moretti, S. Passerini, *ACS Appl. Energy Mater.* **2019**, *2*, 2786; b) Y. Fang, X. Yu, X. Lou, *Angew. Chem., Int. Ed.* **2017**, *56*, 5801
- [5] a) W. Ren, M. Qin, Z. Zhu, M. Yan, Q. Li, L. Zhang, D. Liu, L. Mai, *Nano Lett.* **2017**, *17*, 4713; b) Y. Lu, L. Wang, J. Cheng, J. B. Goodenough, *Chem. Commun. (Camb)* **2012**, *48*, 6544.

- [6] a) P. Barpanda, L. Lander, S. Nishimura, A. Yamada, *Adv. Energy Mater.* **2018**, *8*, 1703055; b) H. Zhang, B. Qin, D. Buchholz, S. Passerini, *ACS Appl. Energy Mater.* **2018**, *1*, 6425.
- [7] Y. Zheng, Y. Wang, Y. Lu, Y. Hu, J. Li, *Nano Energy* **2017**, *39*, 489.
- [8] a) M.-S. Balogun, Y. Luo, W. Qiu, P. Liu, Y. Tong, *Carbon* **2016**, *98*, 162; b) J. Mao, X. Fan, C. Luo, C. Wang, *ACS Appl. Mater. Interfaces* **2016**, *8*, 7147.
- [9] W. Chen, X. Zhang, L. Mi, C. Liu, J. Zhang, S. Cui, X. Feng, Y. Cao, C. Shen, *Adv. Mater.* **2019**, *31*, 1806664.
- [10] S. Foley, H. Geaney, G. Bree, K. Stokes, S. Connolly, M. J. Zaworotko, K. M. Ryan, *Adv. Funct. Mater.* **2018**, *28*, 1800587.
- [11] H. Li, Y. Ma, H. Zhang, T. Diemant, R. J. Behm, A. Varzi, S. Passerini, *Small Methods* **2020**, *4*, 2000637.
- [12] Y. Liu, X.-Y. Yu, Y. Fang, X. Zhu, J. Bao, X. Zhou, X. W. Lou, *Joule* **2018**, *2*, 725.
- [13] X. Hu, Y. Li, G. Zeng, J. Jia, H. Zhan, Z. Wen, *ACS Nano* **2018**, *12*, 1592.
- [14] J. Deng, Q. Gong, H. Ye, K. Feng, J. Zhou, C. Zha, J. Wu, J. Chen, J. Zhong, Y. Li, *ACS Nano* **2018**, *12*, 1829.
- [15] A. Jin, M.-J. Kim, K.-S. Lee, S.-H. Yu, Y.-E. Sung, *Nano Res.* **2019**, *12*, 695.
- [16] Z. Yang, C.-Y. Chen, C.-W. Liu, C.-L. Li, H.-T. Chang, *Adv. Energy Mater.* **2011**, *1*, 259.
- [17] C. Lai, M. Zhang, B. Li, D. Huang, G. Zeng, L. Qin, X. Liu, H. Yi, M. Cheng, L. Li, Z. Chen, L. Chen, *Chem. Eng. J.* **2019**, *358*, 891.
- [18] D. Wang, M. Sun, G. Feng, C. Song, *J. Mater. Eng. Perform.* **2019**, *28*, 6649.
- [19] H. Park, J. Kwon, H. Choi, D. Shin, T. Song, X. W. D. Lou, *ACS Nano* **2018**, *12*, 2827.
- [20] a) B. Qin, A. Schiele, Z. Jusys, A. Mariani, T. Diemant, X. Liu, T. Brezesinski, R. J. Behm, A. Varzi, S. Passerini, *ACS Appl. Mater. Interfaces* **2020**, *12*, 3697; b) K. Li, J. Zhang, D. Lin, D.-W. Wang, B. Li, W. Lv, S. Sun, Y.-B. He, F. Kang, Q.-H. Yang, L. Zhou, T.-Y. Zhang, *Nat. Commun.* **2019**, *10*, 725.
- [21] a) A. Fukunaga, T. Nohira, R. Hagiwara, K. Numata, E. Itani, S. Sakai, K. Nitta, S. Inazawa, *J. Power Sources* **2014**, *246*, 387; b) N. Wongtharom, C. H. Wang, Y. C. Wang, C. H. Yang, J. K. Chang, *ACS Appl. Mater. Interfaces* **2014**, *6*, 17564; c) Q. Wang, L. Jiang, Y. Yu, J. Sun, *Nano Energy* **2019**, *55*, 93.
- [22] S. Fang, G. Wang, L. Qu, D. Luo, L. Yang, S.-I. Hirano, *J. Mater. Chem. A* **2015**, *3*, 21159.
- [23] S. Zhang, K. Xu, T. Jow, *J. Power Sources* **2003**, *113*, 166.
- [24] a) T. Yong, J. Wang, Y. Mai, X. Zhao, H. Luo, L. Zhang, *J. Power Sources* **2014**, *254*, 29; b) J. Wang, T. Yong, J. Yang, C. Ouyang, L. Zhang, *RSC Adv.* **2015**, *5*, 17660.
- [25] Z. Zeng, V. Murugesan, K. S. Han, X. Jiang, Y. Cao, L. Xiao, X. Ai, H. Yang, J.-G. Zhang, M. L. Sushko, J. Liu, *Nat. Energy* **2018**, *3*, 674.
- [26] X. Liu, X. Jiang, Z. Zeng, X. Ai, H. Yang, F. Zhong, Y. Xia, Y. Cao, *ACS Appl. Mater. Interfaces* **2018**, *10*, 38141.
- [27] a) J. K. Feng, X. J. Sun, X. P. Ai, Y. L. Cao, H. X. Yang, *J. Power Sources* **2008**, *184*, 570; b) Z. Zeng, B. Wu, L. Xiao, X. Jiang, Y. Chen, X. Ai, H. Yang, Y. Cao, *J. Power Sources* **2015**, *279*, 6.
- [28] J. Feng, P. Ma, H. Yang, L. Lu, *Electrochim. Acta* **2013**, *114*, 688.
- [29] a) J. Wang, Y. Yamada, K. Sodeyama, E. Watanabe, K. Takada, Y. Tateyama, A. Yamada, *Nat. Energy* **2017**, *3*, 22; b) P. Shi, H. Zheng, X. Liang, Y. Sun, S. Cheng, C. Chen, H. Xiang, *Chem. Commun. (Camb)* **2018**, *54*, 4453.
- [30] a) X. Wang, E. Yasukawa, S. Kasuya, *J. Electrochem. Soc.* **2001**, *148*, 1066; b) X. Wang, C. Yamada, H. Naito, G. Segami, K. Kibe, *J. Electrochem. Soc.* **2006**, *153*, A135.
- [31] a) C.-Y. Chen, T. Kiko, T. Hosokawa, K. Matsumoto, T. Nohira, R. Hagiwara, *J. Power Sources* **2016**, *332*, 51; b) L. Suo, O. Borodin, T. Gao, M. Olguin, J. Ho, X. Fan, C. Luo, C. Wang, K. Xu, *Science* **2015**, *350*, 938.
- [32] Y. He, Z. Chang, S. Wu, Y. Qiao, S. Bai, K. Jiang, P. He, H. Zhou, *Adv. Energy Mater.* **2018**, *8*, 1802130.
- [33] H. Nakagawa, M. Ochida, Y. Domi, T. Doi, S. Tsubouchi, T. Yamanaka, T. Abe, Z. Ogumi, *J. Power Sources* **2012**, *212*, 148.
- [34] X. Jiang, X. Liu, Z. Zeng, L. Xiao, X. Ai, H. Yang, Y. Cao, *Adv. Energy Mater.* **2018**, *8*, 1802176.
- [35] Y. Dong, N. Zhang, C. Li, Y. Zhang, M. Jia, Y. Wang, Y. Zhao, L. Jiao, F. Cheng, J. Xu, *ACS Appl. Energy Mater.* **2019**, *2*, 2708.
- [36] a) Y. Yamada, K. Furukawa, K. Sodeyama, K. Kikuchi, M. Yaegashi, Y. Tateyama, A. Yamada, *J. Am. Chem. Soc.* **2014**, *136*, 5039; b) H. Zhang, S. Jeong, B. Qin, D. V. Carvalho, D. Buchholz, S. Passerini, *ChemSusChem* **2018**, *11*, 1382.
- [37] M. Hu, Z. Ju, Z. Bai, K. Yu, Z. Fang, R. Lv, G. Yu, *Small Methods* **2019**, *4*, 1900673.
- [38] Z. Yang, T. Chen, C. Wu, J. Qu, Z. Wu, X. Guo, B. Zhong, H. Liu, S. Dou, *ACS Appl. Mater. Interfaces* **2019**, *11*, 3961.
- [39] T. Sultana, G. Georgiev, G. Auner, G. Newaz, H. Herfurth, R. Patwa, *Appl. Surf. Sci.* **2008**, *255*, 2569.
- [40] J. Moulder, W. Stickle, P. E. Sobol, K. Bomben, *Handbook of X-ray Photoelectron Spectroscopy*, Perkin-Elmer Corporation, Eden Prairie, MN, USA **1992**.
- [41] G. Gebrekidan, T. Diemant, M. Hekmatfar, S. Grugeong, R. J. Behma, M. Stephane Laruelle, S. Passerini, *Nano Energy* **2019**, *55*, 327.
- [42] G. Murch, R. Thorn, *J. Phys. Chem. Solids* **1980**, *41*, 785.
- [43] Y. Yu, H. Che, X. Yang, Y. Deng, L. Li, Z.-F. Ma, *Electrochem. Commun.* **2020**, *110*, 106635.
- [44] X. Zheng, Z. Gu, X. Liu, Z. Wang, J. Wen, X. Wu, W. Luo, Y. Huang, *Energy Environ. Sci.* **2020**, *13*, 1788.